Measurement 245 (2025) 116651

Contents lists available at ScienceDirect

Measurement

journal homepage: www.elsevier.com/locate/measurement

An ultra-sensitive diamagnetic levitation accelerometer with quasi-zero-stiffness structure

Yang Wang [a], Yuanping Xu [a,*], Lu Yang [b,*], Jin Zhou [a], Jarir Mahfoud [c], Chaowu Jin [a]

[a] College of Mechanical & Electrical Engineering, Nanjing University of Aeronautics and Astronautics, Nanjing 210016, China
[b] College of Civil and Transportation Engineering, Hohai University, Nanjing 210098, China
[c] University of Lyon, INSA-Lyon, CNRS UMR5259, LaMCoS, F-69621 Villeurbanne Cedex, France

ARTICLE INFO

Keywords:
Diamagnetic levitation
Accelerometer
High-sensitivity
Quasi-zero-stiffness structure

ABSTRACT

Ultra-sensitive accelerometers are garnering substantial attention in line with advancements in space physics research. Herein, a novel ultra-sensitive accelerometer based on diamagnetic levitation is proposed by employing a quasi-zero stiffness (QZS) structure of sensitive component. Making use of the QZS structure which consists of dual-layer stacked pyrolytic graphite, the sensitive component demonstrates to be highly sensitive to displacements and maintains the inherit passive self-stabilizing characteristics. The subsequent theoretical and experimental results reveal that by fine-tuning the QZS structure of pyrolytic graphite, an ultra-high sensitivity of 66.84 mm/g can be obtained, which is among the best reported data so far and 9 times higher than that of conventional diamagnetic levitation accelerometer without QZS structure. The extraordinary sensitivity validates the feasibility and effectiveness of QZS structure modulation in boosting sensitivity, presenting a new perspective for developing high-performance diamagnetic levitation accelerometer.

1. Introduction

Over the past decade, the explosive developments in space physics research represented by microgravity measurement and gravitational wave detection, emphasize the demand for discerning ultra-low-frequency weak acceleration signals with ultra-high detection precision [1,2]. To date, high-precision accelerometers rooting in electrostatic levitation, diamagnetic levitation, MEMS (Micro-Electro-Mechanical Systems), cold atom interferometry and other types have been successfully implanted [1,3–8]. Particularly, the diamagnetic levitation type has recently gained special attention on account of the notable yet unique traits including frictionless, low stiffness, and passive self-stabilizing suspension [9–12].

Diamagnetic levitation utilizes the repulsive force between diamagnetic material and magnetic field to achieve stable suspension without physical contact and the need of external input. Making use of the friction-free character, one can dramatically minimize the noise and drift, which is desirable for high-precision measurements [9,10]. Meanwhile, compared with other sensing structure represented by electrostatic levitation or mechanical springs, the diamagnetic levitation systems typically exhibit much lower stiffness, making it highly sensitive to weak and ultra-low-frequency vibrations [11,12]. These characteristics make diamagnetic levitation particularly attractive for constructing ultra-sensitive accelerometers for advancing space physics research.

Based on the diamagnetic levitation mechanism, a few high-precision accelerometers have been reported. For example, D. Garmire et al. proposed a MEMS-based diamagnetic levitation accelerometer, achieving a high resolution of 34 μg and a sensitivity of 0.33 mm/g [3]. B. Andò et al. presented an accelerometer utilizing electromagnetic induction displacement sensing mechanism, permitting a sensitivity of 12 V/g [4]. Wang et al. developed a hybrid levitation accelerometer employing diamagnetic and permanent magnet elements, coupled with optical displacement probes [5]. A maximum sensitivity of 5 mm/g, with residual noise spectrum of 20 $\mathrm{ng}/\sqrt{\mathrm{Hz}}$ at $0.2 \sim 0.3$ Hz, was realized and ensuring its application in detecting seismic wave [5].

Despite the extraordinary and continued progresses achieved for diamagnetic levitation accelerometers, it should be signified that they still suffer from some limitations more or less. Firstly, even the reported sensitivity of diamagnetic levitation accelerometers is comparable to that of electrostatic levitation or MEMS types, it still lags behind the requirements of advanced space physics research. Secondly, current investigation on diamagnetic levitation accelerometers primarily focuses on developing displacement detection methods for sensitive

* Corresponding authors.
E-mail addresses: ypxu@nuaa.edu.cn (Y. Xu), yanglu90@hhu.edu.cn (L. Yang).

https://doi.org/10.1016/j.measurement.2025.116651
Received 2 September 2024; Received in revised form 13 December 2024; Accepted 2 January 2025
Available online 3 January 2025
0263-2241/© 2025 Elsevier Ltd. All rights are reserved, including those for text and data mining, AI training, and similar technologies.

component. However, the resultant sensitivity of diamagnetic levitation accelerometers not only depends on rationally regulating the displacement detection methods, but also strongly relies on the structure of sensitive component. Hence, it is of urgent need to explore optimized structure of sensitive components for developing ultra-sensitive diamagnetic levitation accelerometer.

Recently, a novel quasi-zero stiffness (QZS) structure has been attempted to develop ultra-high sensitivity accelerometers [2,13,14]. Generally, the structure involves combining elements with opposing stiffness characteristics, such as introducing a negative stiffness mechanism onto a positive stiffness structure [15–17]. Making use of this configuration, the global structure remains stable while the stiffness at a specific position can approach zero [16,17]. Consequently, the resistance of sensitive component to deformation or motion can be minimized, making it highly sensitive to displacements. A few high-precision accelerometers based on QZS structure have been proposed [13,18–20]. Take the work conducted by Duan for example, an adjustable QZS accelerometer with a preload force adjustment device was constructed, yielding a maximum sensitivity of 3.8 mm/g [13]. The recent work of Sun also proved that using a three-dimensional (3D) QZS vibration sensor system based on pre-deformed scissor-like structure, one can detect the absolute motion of 3D moving platforms and achieve a maximum sensitivity of 14.9 mm/g [19,20]. Motivated by these works, it is anticipated that the QZS structure can also be used in diamagnetic levitation system to further boost sensitivity [18,21–23]. Theoretically, the inherent passive self-stabilizing characteristics of diamagnetic levitation structure is of great benefit to eliminate complex mechanical connections and control systems to establish QZS structures, making it feasible to realize ideal QZS characteristics under specific magnetic fields and dramatically reducing the fabrication complexity of QZS structures.

Herein, in this work, QZS structure is implemented in diamagnetic levitation accelerometer to evaluate its reinforcing effect in sensitivity for the first time. Specifically, a diamagnetic levitation accelerometer consisting of sensing component and a permanent magnet array, featured with a streamlined design is constructed. The relative vibration between the sensing component and permanent magnet stator is monitored by optical displacement detection approach. Pyrolytic graphite is adopted as the sensitive component and a dual-layer stacked structure of graphite is introduced. Such architecture endows the upper and lower graphite layer with different force characteristics within the undulating magnetic potential well generated by permanent magnet stator. By fine-tuning the shape parameters of the sensitive component, one can guarantee the passive stable levitation of lower graphite layer under positive stiffness magnetic force. Meanwhile, the upper graphite layer would encounter negative stiffness magnetic force. As a consequence, a desirable QZS structure of sensitive component consisting of two graphite layers can be achieved.

A systematic work is performed to elucidate the static suspension characteristics and dynamic response of the accelerometer with QZS structure, with an emphasis on the influencing factors including the shape parameters, suspension height of sensitive component and magnetization parameters of permanent magnet array. The subsequently theoretical and experimental results demonstrate that with the optimized QZS structure, it is facile to induce ideal QZS characteristics by further modulating the magnetization parameters of permanent magnet array and the suspension height of sensitive component. An ultra-high sensitivity of 66.84 mm/g is obtained in this accelerometer, which is among the best reported data so far and 9 times higher than that of conventional diamagnetic levitation accelerometer without QZS structure. For the first time, a pioneering ultra-sensitive diamagnetic levitation accelerometer based on QZS structure is proposed and validated, highlighting the feasibility of structure modulation of sensitive components to boost sensitivity and develop high-performance diamagnetic levitation accelerometer.

2. Structure and principle

The schematic and photos of diamagnetic levitation accelerometer with quasi-zero stiffness (QZS) structure are presented in Fig. 1(a) and (b), respectively. When subjected to vibrations along the radial direction of accelerometer, the sensitive element consisting of two pyrolytic graphite with different diameters, would vibrate radially under inertia. Then, the acceleration signal could be obtained by detecting the relative displacement signal of sensitive element.

For the permanent magnet stator of accelerometer, a unique arrangement of magnets was employed. Specifically, an annular magnet is concentrically arranged around a cylindrical magnet, with the two components having opposite axial magnetization. The cylindrical magnet possesses a radius R_1 of 3.98 mm while the annular permanent magnet has an inner diameter and outer diameter R_2 of 4 mm and 10 mm, respectively. Such arrangement of magnets would enable a wave-like potential well structure manifested in Fig. 1(c). It also should be mentioned that the radial stiffness of two pyrolytic graphite sheets would vary with radius within the wave-like potential well. When the radius of graphite sheet exceeds the radius of central permanent magnet, the radial stiffness at center is positive while the radial stiffness at center is negative once the radius of graphite sheet is smaller than that of central permanent magnet, which would be discussed in the following section 3.2.

For the sensitive element, both pyrolytic graphite layers possess a similar thickness of 0.5 mm while the radius of bottom layer is 5.0 mm and that of upper layer is 3.5 mm. The two pyrolytic graphite layers align along a common central axis and the bottom layer primarily provides axial support to offset gravitational forces. Meanwhile, the bottom layer also delivers positive radial stiffness along the axis, ensuring the passive, stable suspension of sensitive element along the axis direction. Conversely, the upper layer situated within a designated suspension zone, would impart negative radial stiffness. This allows the stiffness of sensitive element at the balance point to be reduced to nearly zero, enabling an optimal near-zero stiffness characteristic.

For the conventional diamagnetic levitation accelerometer, the dynamical equations of a proof mass (sensitive element) can be reduced to an expression for one dimension related to the radial motion [11,24,25].

$$m\ddot{x}_r + c_r\dot{x}_r + k_r x_r = -ma_{base} \tag{1}$$

where m denotes the mass of proof mass, x_r represents the relative displacement between proof mass and stator, a_{base} is the acceleration of base vibration, k_r is the equivalent stiffness calculated from radial diamagnetic force and c_r is the equivalent damping constant calculated from eddy-current effect. By applying the Laplace transform to Eq. (1), we can obtain the transfer function between the input acceleration signal and output displacement signal:

$$X_r(\omega)\Big/A_{base}(\omega) = 1\Big/\omega_n^2\sqrt{\left(1-\left(\frac{\omega}{\omega_n}\right)^2\right)^2+\left[2\zeta\left(\frac{\omega}{\omega_n}\right)\right]^2} \tag{2}$$

where, $\zeta = c_r/\sqrt{mk_r}$ represents the damping ratio and $\omega_n = \sqrt{k_r/m}$represents the natural frequency.

3. Static levitation characteristic

3.1. Diamagnetic levitation

Table 1 lists the basic parameters of proposed accelerometer. According to previous studies, it can be concluded that current model is effective in analyzing the magnetic field of permanent magnets [26–28]. Based on the current model, the cylindrical permanent magnet can be simplified as an equivalent surface current distribution, as illustrated in Fig. 2(a). Meanwhile, it should be noted that in the previous reported

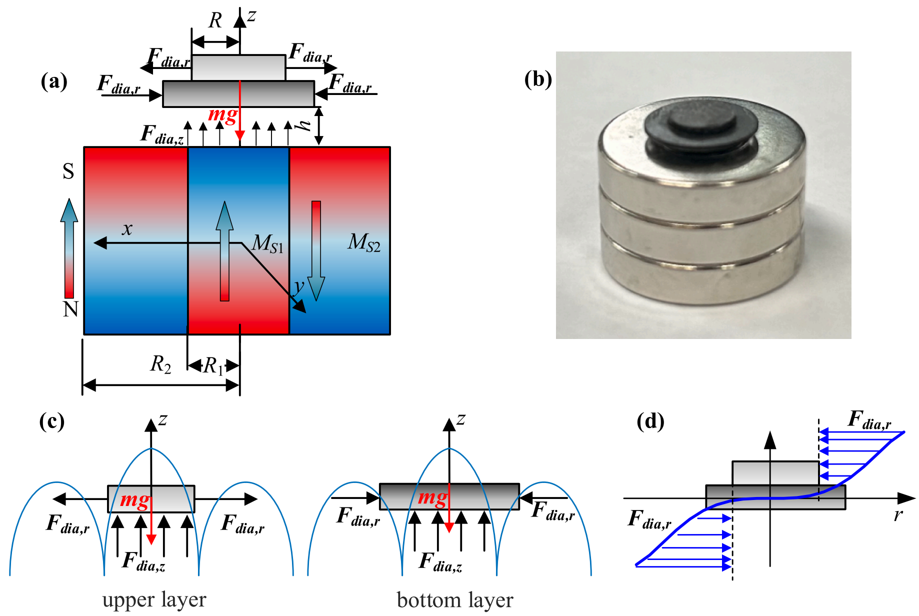

Fig. 1. (a) Schematic diagram of the diamagnetic levitation accelerometer with QZS structure, **(b)** the photos of diamagnetic levitation accelerometer with QZS structure, **(c)** the load characteristics of upper and bottom pyrolytic graphite layers, **(d)** the load characteristic of sensitive element with QZS structure.

Table 1
The basic parameters of the accelerometer.

Parameter	Definition	Value	Unit
R_1	The radius of cylinder magnet	4	Mm
R_2	The radius of annular magnet	10	Mm
L	The length of PM	12	Mm
r_1	The radius of bottom graphite sheet	5	Mm
r_2	The radius of upper graphite sheet	3.5	Mm
h	The levitation height of graphite sheet	0.5	Mm
m	The mass of graphite sheet	105	Mg
Ms_1	The magnetization of cylinder magnet	10×10^5	A/m
Ms_2	The magnetization of annular magnet	10×10^5	A/m
μ_0	The permeability of free space	$4\pi \times 10^{-7}$	Wb/Am
χ_m	The volume magnetic susceptibility of the graphite	-450×10^{-6}	–
B_r	The magnetic flux density along r axis	–	T
B_z	The magnetic flux density along z axis	–	T
$F_{dia,r}$	The diamagnetic force along r axis	–	N
F_{diaz}	The diamagnetic force along z axis	–	N
U_{dia}	The total potential of graphite sheet	–	J/m^3

literatures and this work, the permanent magnets in the diamagnetic levitation system are assumed to be uniformly magnetized along the axis [27].

As shown in Fig. 2, the current distribution is used as the source term in the static electromagnetic field equations, and the magnetic flux density can be obtained using the following formula:

$$\begin{aligned} B_{ir} &= \frac{u_0 M_{si}}{4\pi}\left(\int_{z_1}^{z_2}\int_0^{2\pi}\frac{\cos(\phi-\phi')(z-z')}{|\boldsymbol{P}'-\boldsymbol{P}|^3} r_{i+1} d\phi' dz' \right. \\ &\quad \left. - \int_{z_1}^{z_2}\int_0^{2\pi}\frac{\cos(\phi-\phi')(z-z')}{|\boldsymbol{P}'-\boldsymbol{P}|^3} r_i d\phi' dz'\right) B_{iz} \\ &= \frac{u_0 M_{si}}{4\pi}\left(\int_{z_1}^{z_2}\int_0^{2\pi}\frac{-(r\cos(\phi-\phi')-r_{i+1})}{|\boldsymbol{P}'-\boldsymbol{P}|^3} r_{i+1} d\phi' dz' \right. \\ &\quad \left. - \int_{z_1}^{z_2}\int_0^{2\pi}\frac{-(r\cos(\phi-\phi')-r_i)}{|\boldsymbol{P}'-\boldsymbol{P}|^3} r_i d\phi' dz'\right) \end{aligned} \tag{3}$$

where, $z_1 = 6$ mm, $z_2 =$ -6 mm, P (r,Φ,z) and P' (r',Φ',z') are the point at the surface of magnet and the point in the free space, and the point at the surface of magnet, respectively. $|\boldsymbol{P}-\boldsymbol{P}'| = \sqrt{r^2 + r'^2 - 2rr'\cos(\phi-\phi') + (z-z')^2}$ is the distance between $\boldsymbol{P}$ and $\boldsymbol{P'}$, as shown in Fig. 2(b). r_1, r_2, r_3 represent 0, R_1, R_2 respectively.

As mentioned above, the permanent magnet stator is comprised of an annular magnet concentrically arranged around a cylindrical magnet and the two components possess opposite axial magnetization. Then, the magnetic flux density (B) produced by the permanent magnet at any point in space can be calculated using the following formula:

$$\boldsymbol{B} = \boldsymbol{B}_1 + \boldsymbol{B}_2 \tag{4}$$

where $\boldsymbol{B}_1$ and $\boldsymbol{B}_2$ are the magnetic flux densities generated by cylindrical magnet and annular magnet, respectively. The unit volume potential energy for the diamagnetic material can be then obtained as,

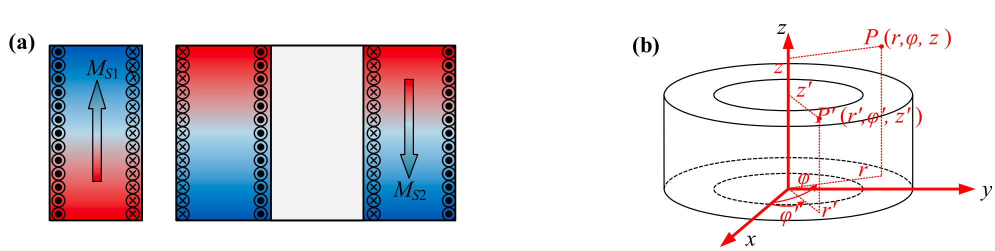

Fig. 2. (a) Distribution of equivalent surface current and **(b)** magnetization of permanent magnet stator.

$$dU_{dia}(r,\varphi,z) = -\frac{\chi_m}{2\mu_0}B^2dV \tag{5}$$

The total potential of the diamagnetic body can be expressed as,

$$U_{total}(r,\varphi,z) = U_{dia} + U_g = \iiint\left(-\frac{\chi_m}{2\mu_0}B^2 + \rho gz\right)dV \tag{6}$$

where ρ is the density of the pyrolytic graphite, and g is the gravity acceleration.

Therefore, the diamagnetic force on the diamagnetic body is found as,

$$\boldsymbol{F_{dia}} = -\nabla U_{dia} = \iiint_V \frac{\chi_m}{2\mu_0}\nabla B^2 dv \tag{7}$$

According to Ostrogradsky theorem, the above equations could be written as,

$$\begin{aligned} \boldsymbol{F}_z &= -\frac{\chi_m}{2\mu_0}\oiint_{S_1+S_2} B^2\hat{n}ds \\ \boldsymbol{F}_r &= -\frac{\chi_m}{2\mu_0}\oiint_{S_3} B^2\hat{r}ds \end{aligned} \tag{8}$$

3.2. The diamagnetic levitation of two distinct layers of pyrolytic graphite

Considering that the magnetic susceptibility of diamagnetic materials in nature is weak ($|\chi_m| < 450 \times 10^{-6}$) and the magnetization of diamagnetic materials rarely affects the external magnetic field, the force characteristics of the sensitive element can be equivalently represented as the diamagnetic forces exerted on two distinct layers of pyrolytic graphite, as shown in Fig. 3.

From formula (8), it can be seen that the diamagnetic force exerted on a single layer of pyrolytic graphite is determined by the suspension height of diamagnetic element, shape parameters, and the magnetization strength of the permanent magnet array. Firstly, the diamagnetic force of sole pyrolytic graphite layer with different radius was analyzed based on formula (8) and the obtained results are shown in Fig. 4. One can see that when the radius of pyrolytic graphite layer exceeds 4 mm, a restorative force directed towards the equilibrium position along the radial direction would be induced. Hence, the pyrolytic graphite layer would exhibit positive stiffness at the equilibrium position and the radial diamagnetic force enables the stable suspension of pyrolytic graphite layer in the radial direction. Once the radius is less than 4 mm, the pyrolytic graphite layer would experience a repulsive force away from the equilibrium position in the radial direction, resulting in negative stiffness at the equilibrium position.

The magnetic potential energy and radial diamagnetic force of upper pyrolytic graphite layer (R = 3.5 mm) and bottom layer (R = 5.0 mm) are presented in Fig. 5. As displayed in Fig. 5(a), the magnetic potential energy of bottom pyrolytic graphite layer would reach a local minimum at the radial center position. Fig. 5(c) gives the radial diamagnetic force of bottom pyrolytic graphite layer when it undergoes radial displacement. It can be seen that when the radial displacement of bottom pyrolytic graphite layer is less than 1.2 mm, the diamagnetic force is directed towards the center and its magnitude increases with increasing radial displacement, demonstrating a positive stiffness effect. This would ensure the subsequently passive stable suspension of sensitive element along the radial axis. For the upper pyrolytic graphite layer, the magnetic potential energy also reaches a local minimum at the radial center position (see Fig. 5(b)). Meanwhile, when the radial displacement of upper pyrolytic graphite layer is less than 0.7 mm, the diamagnetic force would also raise with increasing radial displacement, presenting a negative stiffness effect. As a result, the stiffness of sensitive element would approach zero at the equilibrium position, yielding the ideal quasi-zero stiffness characteristics.

To further elucidate the effect of factors such as suspension height of sensitive element and magnetization strength on the diamagnetic force of sole upper or down pyrolytic graphite layer, a systematic investigation was performed. Shown in Fig. 6(a) and (b) are the diamagnetic force versus radical displacement of bottom and upper pyrolytic graphite layers with varied suspension height *h*, respectively. Apparently, with a suspension height reduced from 1 mm to 0.2 mm, the positive radial stiffness of bottom pyrolytic graphite layer would increase from 0.114 N/m to 0.148 N/m while the negative radial stiffness of upper pyrolytic graphite layer would rise from −0.0546 N/m to −0.283 N/m.

Fig. 6(c) and (d) give the diamagnetic force versus radical displacement of bottom and upper pyrolytic graphite layers with varied magnetization strength of cylindrical magnet (M_{s1}), respectively. With a fixed magnetization strength 1 T of annular magnet (M_{s2}), the positive radial stiffness of bottom pyrolytic graphite layer would slightly varied from 0.158 to 0.137 N/m when M_{s1} increases from 0.8 T to 1.2 T. However, the negative radial stiffness of upper layer would dramatically increase from 0.113 to 0.2515 N/m.

Correspondingly, Fig. 6(e) and (f) present the diamagnetic force versus radical displacement of bottom and upper pyrolytic graphite layers with varied magnetization strength of annular magnet (M_{s2}), respectively. With a fixed M_{s1} of 1 T, the positive radial stiffness of bottom pyrolytic graphite layer would notably rise from 0.103 to 0.203 N/m when M_{s2} increases from 0.8 to 1.2 T. On the other hand, the negative radial stiffness of upper layer would remain to be around 0.181 N/m.

Based on the analysis mentioned above, it can be concluded that M_{s1} primary affects the diamagnetic force of upper pyrolytic graphite layer while M_{s2} strongly affects the diamagnetic force of bottom pyrolytic

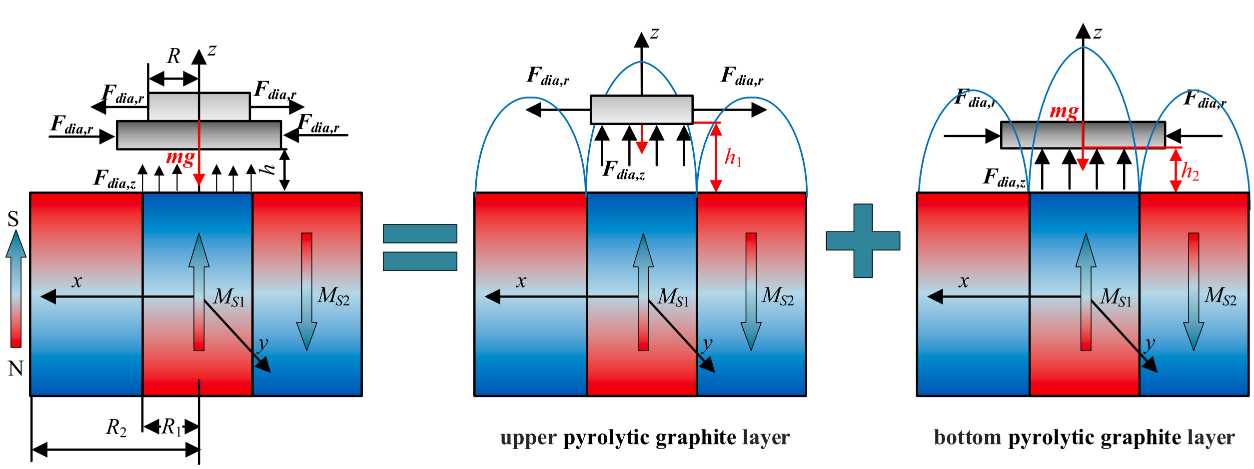

Fig. 3. The schematic diagram of force characteristics of sensitive element, upper and bottom pyrolytic graphite layer.

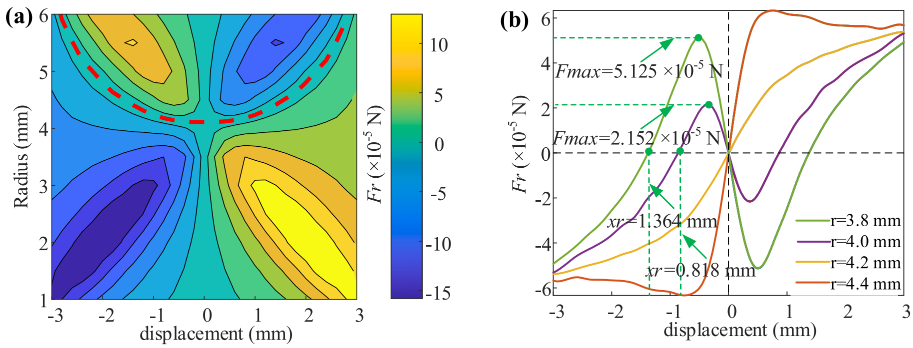

Fig. 4. (a) The diamagnetic force along radial direction versus displacements of pyrolytic graphite layer, **(b)** The diamagnetic force along radial direction versus displacements of pyrolytic graphite layer with varied radius.

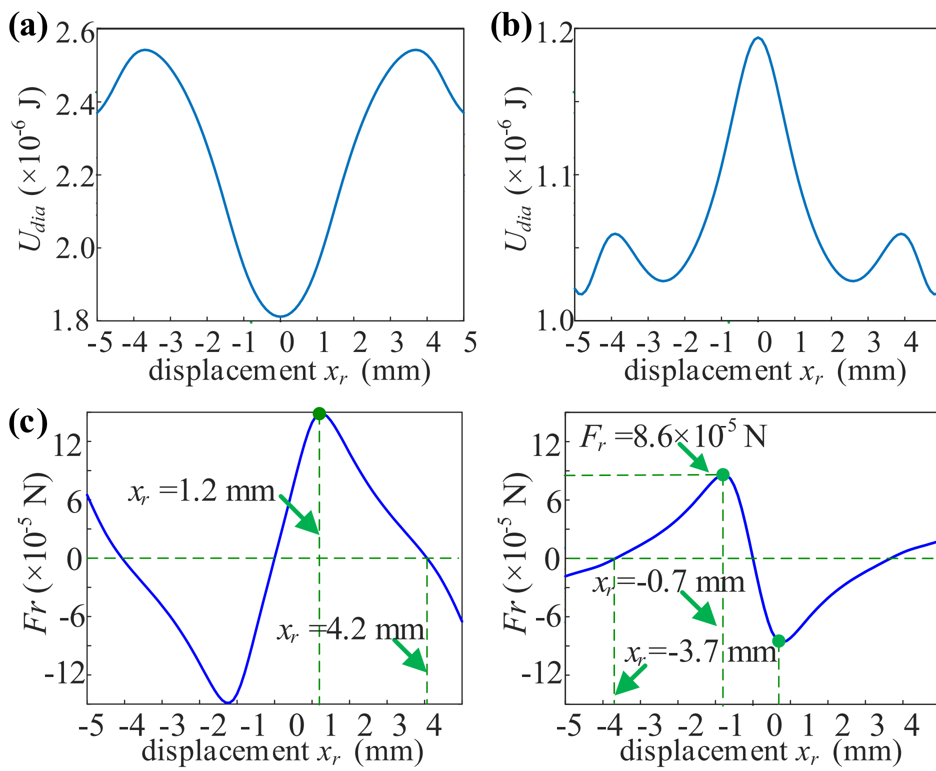

Fig. 5. The magnetic potential energy and diamagnetic force versus radical displacement of **(a, c)** upper pyrolytic graphite layer and **(b, d)** bottom layer.

graphite layer. Given that, the ratio of magnetization strengths of two permanent magnets, namely M_{s1}/M_{s2}, can be adopted to characterize the influence on the quasi-zero stiffness characteristics of this diamagnetic levitation system.

3.3. The diamagnetic levitation of sensitive element

According to the analysis discussed in section 3.2, it can be seen that the upper pyrolytic graphite layer possesses the negative stiffness while the bottom pyrolytic graphite layer delivers the positive stiffness. Thus, the coupling of two layers is of great benefit to enable the passive yet stable suspension of resultant sensitive element and meanwhile significantly minimize the resistance to displacement of sensitive element around the equilibrium point, greatly enhancing the sensitivity of accelerometer. Moreover, by regulating the suspension height of sensitive element and M_{s1}/M_{s2}, one can modulate the quasi-zero stiffness characteristics of diamagnetic levitation system. Fig. 7(a) plots the corresponding suspension height and M_{s1}/M_{s2} in cases wherein ideal quasi-zero stiffness characteristics are obtained. To make it clearer, a typical sample with ideal quasi-zero stiffness characteristic is presented in Fig. 7(b) and (c). In this case wherein $h = 0.18$ mm and $M_{s1}/M_{s2} = 1$, the positive and negative stiffness of the two pyrolytic graphite layers can cancel each other out, resulting in a total stiffness of zero. Additionally, the positive radial stiffness of bottom layer would increase rapidly with increasing displacement, constructing a hard spring characteristic to ensure a wide detection range.

The reported diamagnetic levitation accelerometers are generally based on positive stiffness and thus the relationship between diamagnetic force and displacement of sensitive element at equilibrium position is linearized, as described in Eq. (1) [11,24,25]. However, for the QZS structure, the quasi-zero-stiffness characteristics would induce the nonlinearity of stiffness [16,29]. In this manner, nonlinearity should be considered to describe the relationship between the diamagnetic force and displacement of sensitive element at equilibrium position, as presented in the following equation which adopts a polynomial expression [29].

$$F_r = a_3 x_r^3 + a_2 x_r^2 + a_1 x_r \tag{9}$$

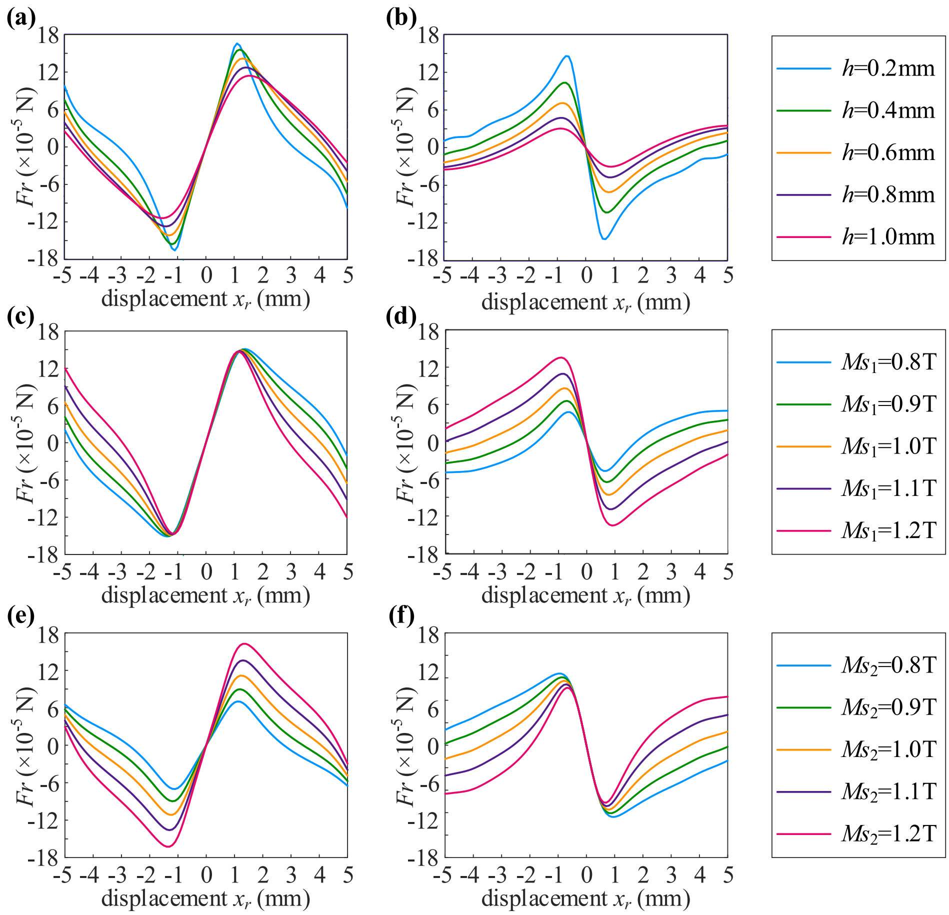

Fig. 6. The diamagnetic force versus radical displacement of bottom and upper pyrolytic graphite layers with **(a, b)** varied h ($M_{s1} = M_{s2} = 1$ T), **(c, d)** varied M_{s1} ($M_{s2} = 1$ T, $h = 0.50$ mm) and **(e, f)** varied M_{s2} ($M_{s1} = 1$ T, $h = 0.5$ mm).

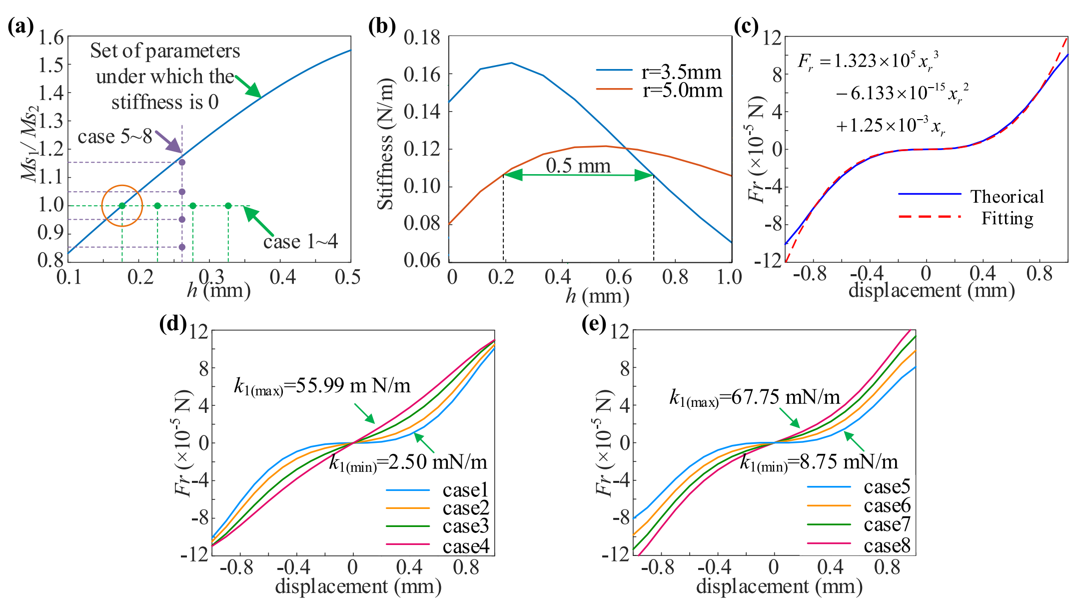

Fig. 7. **(a)** The suspension height and Ms_1/Ms_2 corresponding to ideal quasi-zero stiffness characteristics, **(b)** the stiffness versus h of sensitive element consisting of dual layer of graphite corresponding to case 1, **(c)** the diamagnetic force versus displacement of sensitive element corresponding to case 1, **(d)** the diamagnetic force versus displacement of sensitive element corresponding to case 1–4. **(e)** the diamagnetic force versus displacement of sensitive element corresponding to case 5–8.

where a_1 refers to the linear stiffness, a_2 is square stiffness and a_3 represents the cubic stiffness. When sensitive element is approaching the equilibrium position, the linear stiffness a_1 is mainly responsible for the resultant sensitivity. a_2 would affect the symmetry of diamagnetic force versus displacement curve. It is noted that in this case, a_2 is almost zero due to the axis-symmetric structure of sensitive element and thus can be almost ignored. a_3 would enlarge the radial diamagnetic force considerably when sensitive element is away from the equilibrium position, permitting a wide detection range of accelerometer.

Once the parameters including h or M_{s1}/M_{s2} deviate from the ideal quasi-zero stiffness cases, the sensitive element would then deviate from the ideal quasi-zero stiffness characteristics, as depicted in the cases 1–8 shown in Fig. 7(a). The specific M_{s1}/M_{s2} and suspension heights (h) corresponding to cases 1–8 are detailed in Table 2. Based on Eq. (9), the obtained a_1, a_2, a_3 and R^2 are also given in Table 2. It can be seen that the fitting curves match well with the theoretical curves as the R^2 values are all approaching 1.

Cases 1 to 4 illustrate the gradual departure from quasi-zero stiffness with increasing h. As the h increases from 0.18 mm to 0.33 mm, the quasi-zero stiffness characteristic of the diamagnetic suspension structure gradually weakens. Meanwhile, the linear stiffness at the equilibrium position would rapidly raise from $k_1 = 2.50$ mN/m to $k_1 = 55.99$ mN/m, leading to a rapid decrease in static sensitivity of accelerometer. Cases 5 to 6 describe the gradual deviation from quasi-zero stiffness of diamagnetic suspension system with decreasing M_{s1}/M_{s2}. As the M_{s1}/M_{s2} decreases gradually from 1.15 to 0.85, the quasi-zero stiffness characteristic of diamagnetic suspension structure weakens gradually. The linear stiffness at the equilibrium position would sharply raise from $k_1 = 8.75$ mN/m to $k_1 = 67.75$ mN/m, resulting in a rapid decrease in the static sensitivity of accelerometer.

4 Dynamic performance analysis

4.1. Dynamic response modeling

Given that the detected object undergoes fundamental vibrations under harmonic excitation, the approximate damped vibration equation near the static equilibrium position for QZS diamagnetic levitation accelerometer can be expressed as follows,

$$m\ddot{x}_r + c_r\dot{x}_r + f(x_r) = -mA_{base}cos(\omega t) \tag{10}$$

where m is the mass of the sensitive element, x_r is the relative displacement between the stator and the sensitive element, c is the system's damping and $f(x_r)$is the force–displacement relationship of the system near the equilibrium position. Noted here that c is 6.13×10^{-5} N/(m/s^2) based on the experimental results. Based on the analysis in Section 3.3, $f(x_r)$ can be approximately expressed as $f(x_r) = a_3x_r^3 + a_1x_r$.

To explore the general rules, the time dimension $1/w_n$, the displacement dimension l, and the mass dimension m were adopted to nondimensionalize Eq. (10). The resulting nondimensional parameters are $\widehat{x}_r = \frac{x_r}{l}, \widehat{t} = \omega_n t, \widehat{A}_{base} = \frac{A_{base}}{\omega_n^2 l}, \widehat{\omega} = \frac{\omega}{\omega_n}, \widehat{m} = 1, \zeta = \frac{c}{2m\omega_n}$, and $\widehat{a}_i = \frac{a_i}{a_v}l^{i-1}(i = 1, 2, 3)$, where $\omega_n = \sqrt{k_1/m}$ refers to the undamped natural frequency of system. Therefore, equation (10) can be derived as follows,

$$\ddot{\widehat{x}}_r + 2\zeta\dot{\widehat{x}}_r + \widehat{a}_1\widehat{x}_r + \widehat{a}_3\widehat{x}_r^{\ 3} = \widehat{A}_{base}cos(\widehat{\omega}\widehat{t}) \tag{11}$$

Eq. (11) represents a Duffing equation. Utilizing the Harmonic Balance Method (HBM), when only the system response frequency that aligns with the frequency of simple harmonic excitation is considered while disregarding contributions from higher harmonics, the definitive solution to the equation can thus be represented as shown in Eq. (12).

$$\widehat{x}_r = \widehat{X}_r cos(\omega t + \varphi) \tag{12}$$

By integrating Eqs. (11) and (12) and neglecting the influence of higher harmonics, as well as equalizing the coefficients of corresponding terms, we can determine the steady-state amplitude (x_r) and phase. The sensitive element of accelerometer, under the influence of inertia, generates vibrations that mirror the fundamental vibration acceleration signal. Therefore, the sensitivity of this element is quantifiable through the transfer rate T_d.

$$T_d = \frac{|\widehat{x}_r|}{|\widehat{a}_b \cdot \omega_n^2|} = \frac{1}{\omega_n^2\sqrt{\left(\frac{3}{4}\widehat{a}_3\widehat{X}_r^2 + \widehat{a}_1 - \widehat{\omega}^2\right)^2 + (2\xi\widehat{\omega})}} \tag{13}$$

4.2. Influencing factors

Fig. 8(a) presents the relative displacement response amplitudes of sensitive element with different suspension height upon the vibrations with acceleration amplitude of 4.5 mm/s^2. As shown, with a suspension height of 6.18, 6.23, 6.28 and 6.33 mm, respectively, the corresponding relative displacement response amplitudes of sensitive element are 0.1657 mm, 0.031 mm, 0.017 mm and 0.013 mm, respectively. Fig. 8(b) shows the frequency response curves of QZS accelerometer at different suspension heights. Given the requirements for minimal fluctuations in the frequency response function within the operational range of the accelerometer, its working bandwidth is typically set at one-third of the resonance frequency. The sensitivities corresponding to varied heights are 323.8 mm/g, 65.93 mm/g, 37.28 mm/g, and 26.96 mm/g, respectively. It is observed that by modulating the suspension height of sensitive element and thus approaching/realizing the ideal quasi-zero stiffness characteristics, the sensitivity of the accelerometer can be notably enhanced.

Fig. 9(a) illustrates the relative displacement response amplitudes of sensitive element with different M_{s1}/M_{s2} upon the vibrations with acceleration amplitude of 4.5 mm/s^2. As shown, with the M_{s1}/M_{s2} of 1.15, 1.05, 0.95, and 0.85, respectively, the corresponding relative displacement response amplitudes of sensitive element are 0.081 mm, 0.031 mm, 0.015 mm and 0.010 mm, respectively. Manifested in Fig. 9(b) are the frequency response curves of QZS accelerometer with different M_{s1}/M_{s2}. Given the requirements for minimal fluctuations in the frequency response function within the operational range of the accelerometer, its working bandwidth is typically set at one-third of the resonance frequency. The sensitivities corresponding to varied M_{s1}/M_{s2} are 162.90 mm/g ($M_{s1}/M_{s2} = 1.15$), 61.77 mm/g ($M_{s1}/M_{s2} = 1.05$), 30.54 mm/g ($M_{s1}/M_{s2} = 0.95$) and 19.70 mm/g ($M_{s1}/M_{s2} = 0.85$), respectively. It can also be concluded that by modulating the M_{s1}/M_{s2} and thus approaching/realizing the ideal quasi-zero stiffness characteristics, the sensitivity of the accelerometer can also be dramatically strengthened.

Table 2
The Ms_1/Ms_2, h, corresponding polynomial expression parameters of diamagnetic force (based on Eq. (9) of accelerometer under varied cases.

Case	M_{s1}/M_{s2}	h	a_1	a_2	a_3	R^2
1	1	0.18	0.250e-2	−6.133e-15	1.323e5	0.9965
2	1	0.23	2.258e-2	−5.33e-15	1.173e5	0.9971
3	1	0.28	4.074e-2	−4.472e-15	1.021e5	0.9983
4	1	0.33	5.599e-2	−7.136e-15	8.723e4	0.9994
5	1.15	0.25	0.875e-2	−1.479e-15	8.826e4	0.9932
6	1.05	0.25	2.337e-2	−2.515e-15	8.339e4	0.9965
7	0.95	0.25	4.662e-2	−1.288e-15	7.929e4	0.998
8	0.85	0.25	6.775e-2	−7.509e-16	7.521e4	0.9988

5. Experimental results

5.1. Experimental setup

Fig. 10(a) is the photo of a magnetic field distribution meter for measuring magnetic flux density. Specifically, the permanent magnets are placed on an XY linear motor platform, while the Tesla meter is positioned on a Z-axis precision motion platform. The air gap between the Tesla meter and the permanent magnet increases from 0.6 mm to 3 mm in increments of 0.1 mm. Considering that the Tesla meter can only measure magnetic flux density in the vertical direction, experiments were conducted solely on characterizing Bz. This work used two magnet

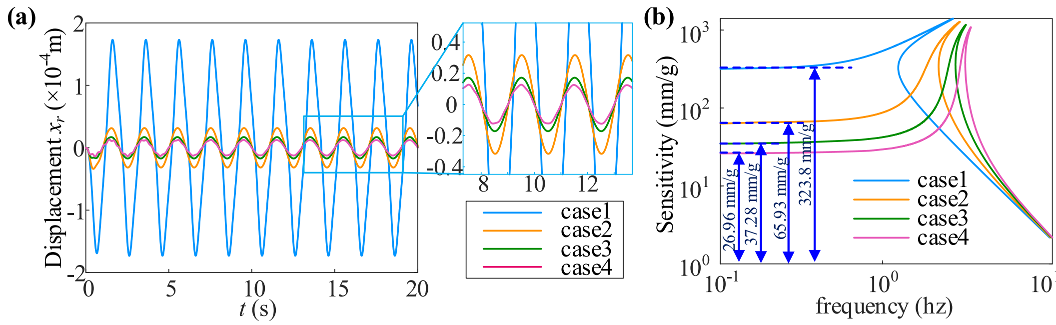

Fig. 8. **(a)** The relative displacement response amplitudes of sensitive element with different suspension height upon the vibrations with acceleration amplitude of 4.5 mm/s^2 (case1-4), **(b)** the frequency response curves of accelerometer at different suspension heights (case1-4).

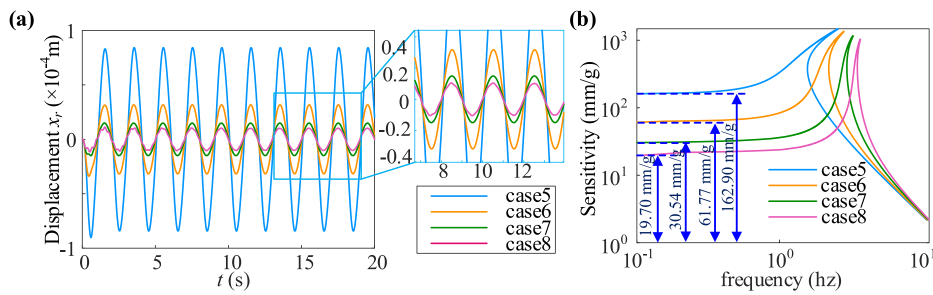

Fig. 9. **(a)** The relative displacement response amplitudes of sensitive element with different M_{s1}/M_{s2} upon the vibrations with acceleration amplitude of 4.5 mm/s^2 (case5-8), **(b)** the frequency response curves of accelerometer with different M_{s1}/M_{s2} (case5-8).

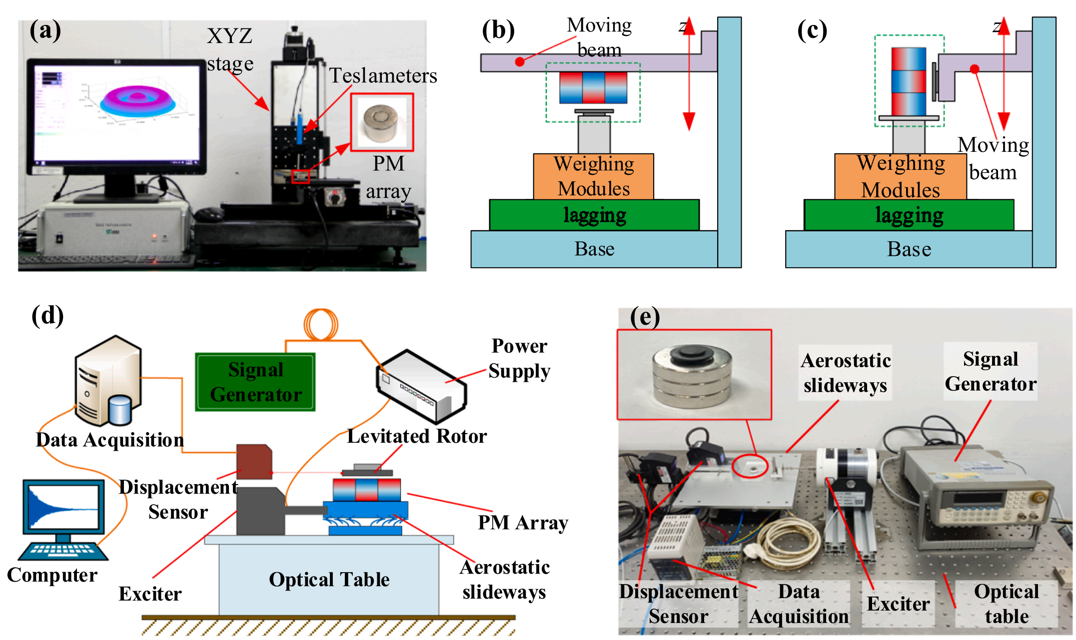

Fig. 10. **(a)**The photo of a magnetic field distribution meter for measuring magnetic flux density, **(b)** the principle of measuring diamagnetic force along the supporting axis, **(c)** the principle of measuring axial diamagnetic force **(d)** the schematic diagrams of experimental setup for comparative calibration tests, **(e)** the photo of experimental setup for comparative calibration tests.

arrays, PM1 and PM2 which possess similar shape and size with different magnetization strength. The peak-to-peak variation curves of magnetic flux density in the plane perpendicular to the axis of the axial magnetic field were recorded, as shown in Fig. 11(a) and (b). For the sake of comparison, the simulation values based on formulas (3) and (4) are also presented in Fig. 11. The experimental magnetization strengths for PM1 are determined to be $M_{s1} = 9.8 \times 10^5$ A/m^3 and $M_{s2} = 8.5 \times 10^5$ A/m^3. For PM2, the experimental $M_{s1} = 8 \times 10^5$ A/m^3 and $M_{s2} = 10.2 \times 10^5$ A/m^3. Clearly, the experimental results are well in accordance with the theoretical values.

Fig. 10(b) and (c) illustrate the principle of measuring diamagnetic force by using a precision scale. When measuring the diamagnetic force along the supporting axis, F_{diaz}, the permanent magnet array was fixed on a stepper motor, which modulated the air gap between the magnet and the diamagnetic component. To eliminate the influence of the magnet on the precision scale, a plastic rod was adopted to support the

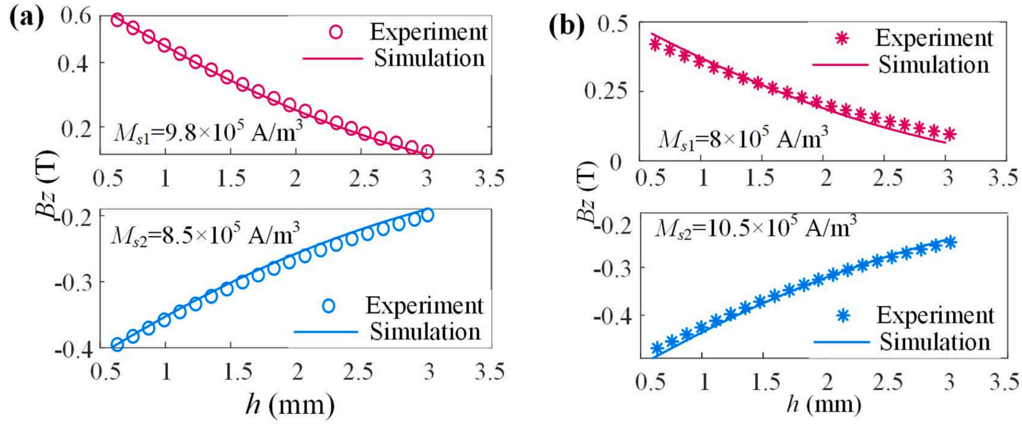

Fig. 11. The experimental and simulated peak-to-peak variation curves of magnetic flux density in the plane perpendicular to the axis of the axial magnetic field for **(a)** PM1 and **(b)** PM2.

diamagnetic component, providing sufficient distance between the magnet and the precision scale. When measuring the axial diamagnetic force, F_{diar}, the permanent magnet array was fixed on a plastic column. The stepper motor was set to descend by 0.1 mm per step, recording the corresponding data until the readings on the scale stabilized. Fig. 12 presents the experimental and simulation curves of axial diamagnetic levitation force with PM1 and PM2 versus suspension height. The suspension height of the sensitive element can be adjusted by attaching a circular thin disk to it, enhancing its quasi-zero stiffness characteristics. A systematic work was performed to dig out the static and dynamic performance of the accelerometer with varied Ms_1/Ms_2 and suspension heights, corresponding to the experiments 1–5 shown in Table 3.

Fig. 10(d) and (e) are the schematic diagrams of experimental setup for comparative calibration tests using dynamic excitation methods. In the calibration experiments, a signal generator produced the excitation signal, which was then amplified by a power amplifier to drive the shaker. Our proposed accelerometer and a reference accelerometer were placed on the same side of shaker. The output signals of the two accelerometers were collected and analyzed by the same FFT analyzer. The proposed accelerometer was securely fixed on a stator connected to the driver, allowing for precise linear vibrations along an air-float rail. The pressure regulating valve was maintained at 0.5 MPa, and the air-float rail utilized the air static pressure effect to stabilize the stator, thereby reducing the friction from basic vibrations and enhancing the fundamental vibration performance of stator.

5.2. The static performances of the proposed accelerometer

Static performances of the proposed accelerometer with varied Ms_1/Ms_2 and suspension heights (experiments 1–5) were first performed to validate the effectiveness of QZS in modulating sensitivity. The obtained diamagnetic force along the supporting axis, F_{diaz} and corresponding $K1$ are displayed in Fig. 13(a) and (b), respectively. Also, the theoretical diamagnetic force is also plotted in Fig. 13, revealing the good accordance between theoretical and experimental results.

By comparing the results corresponding to experiments 1 and 2, it can be observed that with the same stator (PM1), the stiffness at the equilibrium position of sensitive element would decrease from 0.070 N/m to 0.025 N/m when suspension height was reduced from 0.59 mm to 0.41 mm. Meanwhile, by comparing the results corresponding to experiments 1 and 3, one can see that with the same sensitive element (m = 0.208 g), the stiffness at the equilibrium position would decrease from 0.090 N/m to 0.025 N/m when changing the stator from PM2 (M_{s1}/M_{s2} = 1.152) to PM1 (M_{s1}/M_{s2} = 0.76). The results demonstrate that the quasi-zero stiffness characteristics can be yielded by adjusting the suspension height and M_{s1}/M_{s2}.

Moreover, based on the results shown in experiment 5, it is clear that the stiffness at the equilibrium position of the sensitive element was 0.170 N/m when using a single pyrolytic graphite layer and PM1 for conventional diamagnetic levitation accelerometer. However, the dual-layered structure of pyrolytic graphite layers enables much lower stiffnesses, i.e., 0.025 N/m, 0.070 N/m at the equilibrium position, revealing the feasibility of simple dual-layered structure in constructing QZS and reducing stiffnesses.

5.3. The dynamic performances of the proposed accelerometer

The dynamic performances of the proposed accelerometer with varied Ms_1/Ms_2 and suspension heights (experiments 1–5) were also carried out. Fig. 14(a) gives the experimental frequency response curves

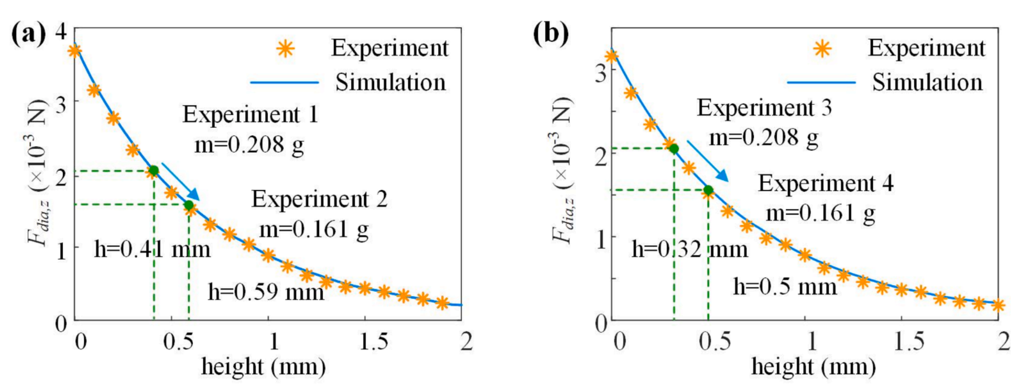

Fig. 12. The experimental and theoretical axial diamagnetic levitation force with **(a)** PM1 and **(b)** PM2 versus suspension height.

Table 3
The Ms_1/Ms_2, suspension heights (*h*) and sensitivity of accelerometer under varied experiments.

Experiment	m (g)	Magnetization ($\times 10^5$ A/m^3)		*h* (mm)	a_1 (N/m)	Sensitivity (mm/g)	
		M_{s1}	M_{s2}			Simulation	Sensitivity
1	0.208	9.8	8.5	0.41	0.025	81.53	66.84
2	0.161	9.8	8.5	0.59	0.070	22.54	23.4
3	0.208	8	10.5	0.32	0.090	22.64	24.6
4	0.161	8	10.5	0.5	0.114	13.84	16.5
5	0.112	9.8	8.5	6.25	0.170	6.86	7.1

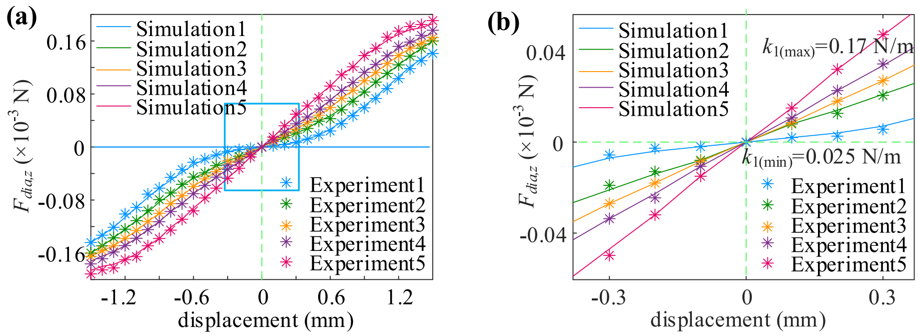

Fig. 13. **(a)** The experimental and theoretical diamagnetic force along supporting axis, F_{diaz} versus displacement for accelerometer, **(b)** The experimental and theoretical diamagnetic force along supporting axis, F_{diaz} around the equilibrium position.

of accelerometer with different Ms_1/Ms_2 and suspension heights. By comparing the results corresponding to experiments 1 and 2, it can be observed that with the same stator (PM1), the sensitivity at the equilibrium position of sensitive element would increase from 23.4 mm/g to 66.84 mm/g when suspension height was reduced from 0.59 mm to 0.41 mm. Meanwhile, by comparing the results corresponding to experiments 1 and 3, one can see that with the same sensitive element (m = 0.208 g), the stiffness at the equilibrium position would enhance from 24.6 mm/g to 66.84 mm/g when changing the stator from PM2 ($M_{s1}/M_{s2} = 1.152$) to PM1 ($M_{s1}/M_{s2} = 0.76$). The results demonstrate that the quasi-zero stiffness characteristics can also be yielded by adjusting the suspension height and M_{s1}/M_{s2}, consequently enhancing the sensitivity.

Furthermore, based on the results shown in experiment 5, the sensitivity of accelerometer was only 7.1 mm/g based on single-layered sensitive element and PM1. However, sensitivity of accelerometer based on QZS can reach up to 66.84 mm/g, which is over 9 times that of convention diamagnetic levitation accelerometer. It is worthy noting that even the mass increment of sensitive element would be of benefit to enhance the sensitivity when adjusting the suspension height, the enhancement in sensitivity is rather slight.

Meanwhile, based on the dynamic modeling equation, the theoretical frequency response curves of accelerometer can also be obtained and the theoretical curves are plotted in Fig. 14(b). Evidently, the theoretical frequency response curves fit well the experimental curves, ensuring the good agreement between theoretical and experimental sensitivities.

The sensitivity of proposed accelerometer is also compared with the recent works concerning high-sensitivity accelerometers [1,12–14,18,22,30–32]. As shown in Fig. 15, it can be concluded that the optimized QZS structured accelerometer possesses a low natural frequency of 1.8 Hz, permitting an ultra-high sensitivity that outperforms the reported diamagnetic levitation types and even is comparable with those reported in ultra-high sensitivity MEMS accelerometer [[1,12–14,18,22,30–32].

6. Conclusion

In this work, QZS structure is employed in diamagnetic levitation accelerometer to evaluate its reinforcing effect on sensitivity for the first time. Making use of a simple dual-layer stacked structure of graphite in sensitive element, an ideal QZS structure is constructed. A comprehensive study was performed to explore the static and dynamic responses of the proposed accelerometers with QZS structure, with an emphasis on digging out the influences of shape parameters, suspension height of sensitive element, and magnetization characteristics of the permanent magnets. The theoretical and experimental validate that by optimizing

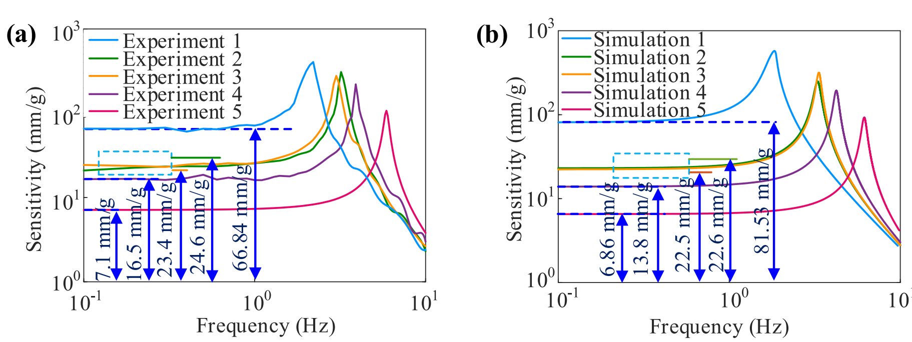

Fig. 14. **(a)** The experimental frequency response curves of accelerometer with different Ms_1/Ms_2 and suspension heights, **(b)** The theoretical frequency response curves of accelerometer with different Ms_1/Ms_2 and suspension heights.

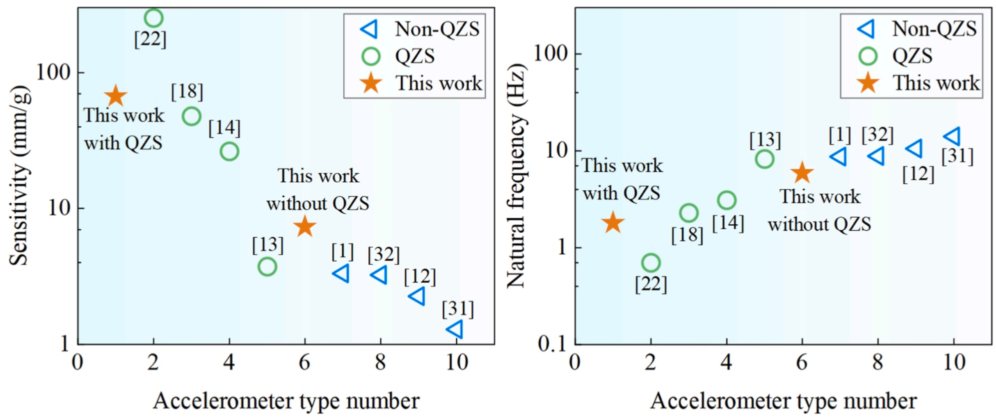

Fig. 15. (a) Sensitivity and (b) natural frequency comparisons among different types of accelerometers with high sensitivities.

the QZS structure and adjusting magnetization of magnets and the suspension height, one can achieve ideal QZS properties. The QZS characteristics endow the proposed accelerometer with an exceptional sensitivity of 66.84 mm/g, which is among the highest reported data so far and almost tenfold greater than conventional non-QZS diamagnetic levitation accelerometers. This work reveals the feasibility of QZS in constructing ultra-sensitive diamagnetic levitation accelerometer, providing a new perspective for developing high-performance diamagnetic levitation accelerometer.

CRediT authorship contribution statement

Yang Wang: Writing – original draft, Project administration, Methodology, Conceptualization. **Yuanping Xu:** Resources, Conceptualization. **Lu Yang:** Writing – original draft, Project administration, Methodology, Conceptualization. **Jin Zhou:** Writing – review & editing, Methodology. **Jarir Mahfoud:** Data curation, Writing – review & editing. **Chaowu Jin:** Writing – review & editing, Validation.

Declaration of competing interest

The authors declare that they have no known competing financial interests or personal relationships that could have appeared to influence the work reported in this paper.

Acknowledgments

The authors gratefully acknowledge the support of the National Natural Science Foundation of China (Grant Numbers 52275537) and the International Joint Laboratory of Sustainable Manufacturing, Ministry of Education and the Fundamental Research Funds for the Central Universities (Grant Numbers NG2024006).

Data availability

Data will be made available on request.

References

[1] F. Han, B. Sun, L. Li, Wu. Qiuping, Performance of a sensitive micromachined accelerometer with an electrostatically suspended proof mass, IEEE Sens. J. 15 (2015) 209–217, https://doi.org/10.1109/JSEN.2014.2340862.

[2] Y. Guo, Z. Ma, T. Zhang, Y. Jin, X. Zheng, Z. Jin, Stabilization control of a MEMS accelerometer with tuned quasi-zero stiffness, IEEE Sens. J. 21 (2021) 27361–27373, https://doi.org/10.1109/JSEN.2021.3126020.

[3] D. Garmire, H. Choo, R. Kant, S. Govindjee, C.H. Sequin, R.S. Muller, J. Demmel, Diamagnetically levitated MEMS accelerometers, in: TRANSDUCERS 2007–2007 International Solid-State Sensors, Actuators and Microsystems Conference, IEEE, Lyon, 2007, pp. 1203–1206, https://doi.org/10.1109/SENSOR.2007.4300352.

[4] B. Ando, S. Baglio, V. Marletta, A. Valastro, A. Pistorio, C. Trigona, A friction less accelerometer exploiting a magnetic levitating mechanism and an inductive readout strategy, in: 2017 IEEE International Instrumentation and Measurement Technology Conference (I2MTC), IEEE, Torino, Italy, 2017, pp. 1–5, doi: 10.1109/I2MTC.2017.7969961.

[5] Q. Wang, X. Ren, S. Jiao, X. Lei, S. Zhang, H. Liu, P. Luo, L. Tu, A diamagnetic levitation based inertial sensor for geophysical application, Sens. Actuators, A 312 (2020) 112122, https://doi.org/10.1016/j.sna.2020.112122.

[6] Z. Qu, H. Ouyang, W. Xiong, Q. Xu, Y. Wang, H. Liu, A nano-g MOEMS accelerometer featuring electromagnetic force balance with 157-dB dynamic range, IEEE Trans. Ind. Electron. 71 (2024) 6418–6426, https://doi.org/10.1109/TIE.2023.3294597.

[7] A. Trimeche, B. Battelier, D. Becker, A. Bertoldi, P. Bouyer, C. Braxmaier, E. Charron, R. Corgier, M. Cornelius, K. Douch, N. Gaaloul, S. Herrmann, J. Müller, E. Rasel, C. Schubert, H. Wu, F. Pereira Dos Santos, Concept study and preliminary design of a cold atom interferometer for space gravity gradiometry, Class. Quantum Grav. 36 (2019) 215004, https://doi.org/10.1088/1361-6382/ab4548.

[8] Q. Lu, Y. Wang, X. Wang, Y. Yao, X. Wang, W. Huang, Review of micromachined optical accelerometers: from mg to sub-μg, OEA 4 (2021) 200045–200045, doi: 10.29026/oea.2021.200045.

[9] Ch. Pigot, B. Delinchant, G. Poulin, G. Reyne, Optimization of a 3D micro-accelerometer based on diamagnetic levitation, Int. J. Appl. Electromagn. Mech. 30 (2009) 179–188, https://doi.org/10.3233/JAE-2009-1020.

[10] Y. Leng, Y. Chen, R. Li, L. Wang, H. Wang, L. Wang, H. Xie, C.-K. Duan, P. Huang, J. Du, Measurement of the earth tides with a diamagnetic-levitated micro-oscillator at room temperature, Phys. Rev. Lett. 132 (2024) 123601, https://doi.org/10.1103/PhysRevLett.132.123601.

[11] Y. Xu, Q. Jiang, K. Yang, J. Zhou, Q. Guo, A novel ultra-high-resolution inclination sensor based on diamagnetic levitation, Sens. Actuators, A 343 (2022) 113686, https://doi.org/10.1016/j.sna.2022.113686.

[12] F. Xiong, P. Yin, T. Wu, H. Xie, R. Li, Y. Leng, Y. Li, C. Duan, X. Kong, P. Huang, J. Du, Lens-free optical detection of thermal motion of a sub-millimeter sphere diamagnetically levitated in high vacuum, Phys. Rev. Appl. 16 (2021) L011003, https://doi.org/10.1103/PhysRevApplied.16.L011003.

[13] Y. Duan, X. Wei, H. Wang, M. Zhao, Z. Ren, H. Zhao, J. Ren, Design and numerical performance analysis of a microgravity accelerometer with quasi-zero stiffness, Smart Mater. Struct. 29 (2020) 075018, https://doi.org/10.1088/1361-665X/ab8838.

[14] S. Tang, H. Liu, S. Yan, X. Xu, W. Wu, J. Fan, J. Liu, C. Hu, L. Tu, A high-sensitivity MEMS gravimeter with a large dynamic range, Microsyst. Nanoeng. 5 (2019) 45, https://doi.org/10.1038/s41378-019-0089-7.

[15] T. Liu, A. Li, H. Zhang, Quasi-zero stiffness interval optimization design and dynamics analysis of a new bi-directional horizontal isolation system, Mech. Syst. Sig. Process. 206 (2024) 110852, https://doi.org/10.1016/j.ymssp.2023.110852.

[16] G. Gatti, A nonlinear quasi-zero stiffness vibration isolator with quintic restoring force characteristic: a fundamental analytical insight, J. Vib. Control 30 (2024) 4185–4198, https://doi.org/10.1177/10775463231205806.

[17] W.H. Qi, G. Yan, J.J. Lu, F.R. Liu, T.Y. Zhao, H. Yan, W.M. Zhang, Local gravity control method for solving load-mismatch issue in isolators, Int. J. Mech. Sci. 265 (2024) 108891, https://doi.org/10.1016/j.ijmecsci.2023.108891.

[18] R.P. Middlemiss, A. Samarelli, D.J. Paul, J. Hough, S. Rowan, G.D. Hammond, Measurement of the earth tides with a MEMS gravimeter, Nature 531 (2016) 614–617, https://doi.org/10.1038/nature17397.

[19] X. Sun, X. Jing, L. Cheng, J. Xu, A 3-D quasi-zero-stiffness-based sensor system for absolute motion measurement and application in active vibration control, IEEE/ASME Trans. Mechatron. 20 (2015) 254–262, https://doi.org/10.1109/TMECH.2014.2338932.

[20] X. Jing, Y. Wang, Q. Li, X. Sun, Design of a quasi-zero-stiffness based sensor system for the measurement of absolute vibration displacement of moving platforms, Smart Mater. Struct. 25 (2016) 097002, https://doi.org/10.1088/0964-1726/25/9/097002.

[21] T. Wu, R. Xiong, X. Xu, Y. Liu, S. Du, L. Jin, F. Chen, A miniaturized MEMS accelerometer with anti-spring mechanism for enhancing sensitivity, (2024), doi: 10.21203/rs.3.rs-4519394/v1.

[22] W. Wu, D. Liu, H. Liu, S. Yan, S. Tang, J. Liu, F. Hu, J. Fan, L. Tu, Measurement of tidal tilt by a micromechanical inertial sensor employing quasi-zero- stiffness mechanism, J. Microelectromech. Syst. 29 (2020) 1322–1331, https://doi.org/10.1109/JMEMS.2020.3001928.

[23] H. Hussein, C. Wang, R. Amendoeira Esteves, M. Kraft, H. Fariborzi, Near-zero stiffness accelerometer with buckling of tunable electrothermal microbeams, Microsyst. Nanoeng. 10 (2024) 43, https://doi.org/10.1038/s41378-024-00657-w.

[24] X. Chen, S.K. Ammu, K. Masania, P.G. Steeneken, F. Alijani, Diamagnetic Composites for high-Q levitating resonators, Adv. Sci. 9 (2022) 2203619, https://doi.org/10.1002/advs.202203619.

[25] G. Aydemir, A. Kosar, H. Uvet, Design and implementation of a passive micro flow sensor based on diamagnetic levitation, Sens. Actuators, A 300 (2019) 111621, https://doi.org/10.1016/j.sna.2019.111621.

[26] Y. Xu, Y. Zhang, J. Zhou, C. Jin, Modeling and validation of diamagnetic rotor levitated by permanent magnetics, Chin. J. Mech. Eng. 37 (2024) 67, https://doi.org/10.1186/s10033-024-01053-1.

[27] J.-Y. Chen, J.-B. Zhou, G. Meng, W.-M. Zhang, Evaluation of Eddy-current effects on diamagnetic bearings for microsystems, IEEE Trans. Ind. Electron. 56 (2009) 964–972, https://doi.org/10.1109/TIE.2008.2011346.

[28] E.P. Furlani, Chapter 3 - field analysis, in: E.P. Furlani (Ed.), Permanent Magnet and Electromechanical Devices, Academic Press, San Diego, 2001, pp. 97–205, https://doi.org/10.1016/B978-012269951-1/50004-8.

[29] M.F. Daqaq, R. Masana, A. Erturk, D. Dane Quinn, On the role of nonlinearities in vibratory energy harvesting: a critical review and discussion, Appl. Mech. Rev. 66 (2014) 040801, https://doi.org/10.1115/1.4026278.

[30] H.-F. Liu, Z.-C. Luo, Z.-K. Hu, S.-Q. Yang, L.-C. Tu, Z.-B. Zhou, M. Kraft, A review of high-performance MEMS sensors for resource exploration and geophysical applications, Pet. Sci. 19 (2022) 2631–2648, https://doi.org/10.1016/j.petsci.2022.06.005.

[31] W. Wu, J. Liu, J. Fan, D. Peng, H. Liu, L. Tu, A nano-g micromachined seismic sensor for levelling-free measurements, Sens. Actuators, A 280 (2018) 238–244, https://doi.org/10.1016/j.sna.2018.07.050.

[32] C. Li, Z. Sun, L. Zhou, X. Zheng, X. Guo, X. Huang, B. Yang, Microseismic observation enabled by high-sensitivity micromechanical interferometers, IEEE Trans. Ind. Electron. 71 (2024) 5349–5359, https://doi.org/10.1109/TIE.2023.3283713.